Composites Part B 148 (2018) 114–122

Contents lists available at ScienceDirect

Composites Part B

journal homepage: www.elsevier.com/locate/compositesb

Instabilities and pattern formations in 3D-printed deformable fiber composites

Jian Li[a], Viacheslav Slesarenko[a], Pavel I. Galich[a], Stephan Rudykh[b,*]

[a] Faculty of Aerospace Engineering, Technion – Israel Institute of Technology, Haifa 32000, Israel
[b] Department of Mechanical Engineering, University of Wisconsin – Madison, Madison, WI 53706, USA

ARTICLE INFO

Keywords:
Instability
Pattern formation
Fiber composite
Finite deformation

ABSTRACT

We investigate elastic instabilities and pattern formations in 3D-printed deformable fiber composites. We experimentally realize the instability induced patterns in the deformable 3D systems of periodically distributed fibers embedded in soft matrix. We observe that the fiber composites exhibit significant softening upon achieving the critical strain at which the stiff fibers cooperatively buckle into wavy patterns. For periodically distributed fiber composites with square in-plane periodicity, we observe the transition of the instability induced patterns from small wavelength wavy pattern to long wave mode with an increase in fiber volume fraction. Both experimental results and rigorous Bloch-Floquet numerical analysis show that the critical wavenumber and critical strain decrease with an increase in fiber volume fraction. For composites with rectangular in-plane periodicity of fibers, we observe that the cooperative buckling mode develops in the direction, where the fibers are close to each other; and an increase in the periodicity aspect ratio leads to a decrease in critical wavenumber and critical strain. In addition, we present our theoretical, numerical, and experimental results for single fiber in soft matrix system. For the single fiber system, we observe that the critical wavelength has a linear dependence on fiber diameter. An explicit formula is derived to estimate the dependence of critical wavelength on shear modulus contrast, and further verified by experimental data and numerical simulations.

1. Introduction

Elastic stiff fibers embedded in a soft matrix are ubiquitous in natural and synthetic systems, e.g., microtubules in living cell [1,2], fibrous biological tissues [3,4], and fiber-reinforced polymer composites [5–8]. It is well known that an isolated fiber experiences classical Euler buckling, when subjected to axial compressive loads. However, for stiff fibers embedded in a soft matrix, the presence of soft matrix significantly decreases the critical wavelength and increases the critical strain [2,9,10]. This mechanical phenomena has drawn considerable attention, due to its importance in fiber composite designs [11–14], functional material designs [15,16], and biological systems [3,17].

The buckling behavior of a single stiff circular wire embedded in an elastic matrix was firstly theoretically investigated by Herrmann et al. [18], which considered the elastic matrix as a three-dimensional continuous body and proposed two foundation model to investigate the buckling behavior of the stiff wire: (a) exact foundation model that considered the displacement and force continuity requirements between the elastic matrix and the stiff wire, (b) approximate foundation model that only considered the displacement and force in radial direction and neglected the shear deformation between the elastic matrix and the stiff wire. For the approximate mode, Herrmann et al. [18] derived an explicit expression to estimate the stiffness of the matrix. Later, Brangwynne et al. [2] employed Herrmann's approximate foundation model to elucidate their experimental observations on the buckling of microtubules in living cells, and derived an expression to approximate the value of matrix stiffness. Recently, Su et al. [19] studied the buckling behavior of a slender Nitinol rod embedded in a soft elastomeric matrix. Planar wavy patterns and non-planar coiled buckling modes were experimentally observed; these experimental observations were interpreted based on consideration of the two lowest buckling modes. Zhao et al. [10] examined the buckling of finite length elastic fiber in a soft matrix; the authors derived a formula to connect the overall strain and the strain state in stiff fiber. This formula showed that the buckling of stiff fiber could be significantly tuned by the slenderness ratio of the fiber. More recently, Chen et al. [20] examined the buckling of stiff wire in soft matrix, and numerically showed that the stiff wire buckled in 2D sinusoidal configuration first, then gradually transited the configuration from 2D sinusoidal into 3D helical mode. In many studies, Winkler foundation model [21] is used to

* Corresponding author.
E-mail address: rudykh@wisc.edu (S. Rudykh).

https://doi.org/10.1016/j.compositesb.2018.04.049
Received 28 January 2018; Received in revised form 18 April 2018; Accepted 24 April 2018
Available online 28 April 2018
1359-8368/

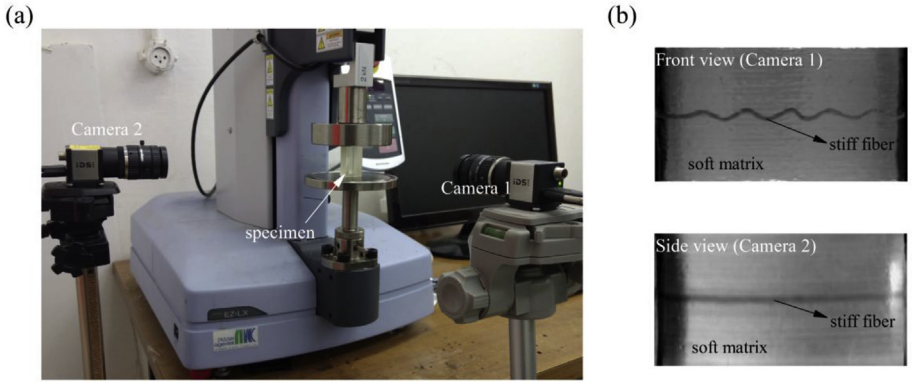

Fig. 1. Experimental setup (a) and typical buckled configurations (b).

provide analytical linear elasticity based estimates for buckling of a single fiber in matrix. However, the accuracy of this model in a wide range shear modulus contrast is not examined. Here, we first experimentally observe the buckling process of a stiff fiber embedded in a soft matrix under an axial compressive load by 3D printer fabricated specimens, and show the dependence of the critical wavelength on the stiff fiber diameter. Then, based on the Wrinker foundation model, we mathematically derive a new estimation for the effective stiffness, and give an explicit formula to calculate the critical wavelength of the stiff fiber in this system. The accuracy of this formula is verified by experimental data and numerical simulations.

The pioneering work on the stability analysis of layered and fiber composites was laid by Rosen [22], who derived an explicit expression to predict the buckling strain of layered composite with linear elastic material. Triantafyllidis and Maker [23] investigated microscopic and macroscopic instabilities in periodic layered composites with hyperelastic phases. Geymonant et al. [24] established rigorous theoretical foundation for microscopic instability analysis in periodic composites, connecting the specific case of long wave limit and the macroscopic loss of ellipticity analysis. The loss of ellipticity analysis has been used to study macroscopic instability in fiber-reinforced hyperelastic solids based on phenomenological models [25–28]. An alternative approach of micromechanics based homogenization was utilized to estimate the macroscopic instabilities in transversely isotropic hyperelastic fiber composite [29,30]. Recently, Greco et al. [31] investigated the influence of matrix or fiber/matrix interface microcracks on the failure behaviors of periodic fiber-reinforced composites under biaxial loading conditions. By making use of the Bloch-Floquet analysis superimposed on large deformations, Slesarenko and Rudykh [13] analyzed the interplay between macroscopic and microscopic instabilities in periodic hyperelastic 3D fiber composites subjected to an axial compressive load. Moreover, the buckling modes with wavy patterns in periodic layered composites under compressive loads were observed in experiments [32,33]. However, to the best of our knowledge, instabilities of deformable periodic 3D fiber composite has not been experimentally investigated. In this paper, we study the buckling behavior of periodic 3D fiber composites with square and rectangular arrangements of periodic fibers; to this end we utilize a multimaterial 3D printer, and fabricate and mechanically test the periodic composite specimens. The experimentally obtained critical wavelengths and critical strains are compared with numerical results by Bloch-Floquet analysis.

The paper is structured as follows: Section 2 presents the introduction for the fabrication of specimens, experimental device and setup. The experimental investigation and theoretical analysis of buckling of a single fiber embedded in a soft matrix are given in Section 3. Section 4 is devoted to instability induced pattern formations in periodic fiber. Section 4.1 presents the results for fiber composites with periodic square arrangement, and Section 4.2 focuses on fiber composites with periodic rectangle arrangement. Section 5 concludes the study with a summary and discussion.

2. Experiment method

2.1. Specimen fabrication

To experimentally observe the buckling process of fiber composite subjected to uniaxial compression along the fibers, we fabricated the specimens composed of stiff fibers embedded in an elastomeric soft matrix by using the multi-material 3D printer Object Connex 260-3. The soft matrix was printed in TangoPlus (TP) with the initial shear modulus $G \approx 0.23$ MPa, the stiffer fiber was printed in a digital material (DM) with the initial shear modulus $G \approx 240$ MPa; the digital material is a mixture of the two base material (TangoPlus and VeroWhite). Here, we considered two cases: single stiff fiber embedded in a soft matrix (Case A); periodic fiber composites with square and rectangle arrangements (Case B). All the specimens were printed in the shape of rectangular blocks to provide a clearer visualization of the buckled fiber shapes and pattern formations through the nearly transparent soft matrix material. Guided by the theoretical and numerical predictions of the buckling wavelength of the stiff fiber and considering the resolution of the multi-material 3D printer, the samples composed of a centrally located single DM fiber embedded in TP matrix (case A) were printed in dimensions $20 \times 20 \times 40$ mm (length × width × height) and in stiff fiber diameters ranging from $d = 0.5$–1.0 mm; the samples composed of 36 periodically distributed fibers embedded TP matrix (case B) were printed in dimensions $30 \times 30 \times 40$ mm (length × width × height) and in stiff fiber volume fractions ranging from $c_f = 0.01$ to 0.025, except for the sample with $c_f = 0.025$, whose height was printed in 50 mm. For the composites with periodically distributed fibers, to reduce the influence of boundary effects on the buckling behavior of stiff fibers, the samples were printed with a boundary TP material layer of the thickness $t = 5$ mm.

2.2. Experimental setup

The uniaxial compression tests were carried out using Shimadzu EZ-LX testing machine (maximum load 2 kN). Fig. 1 shows the experiment setup of the uniaxial compression of 3D-printed samples (a), and an illustration of the buckled configurations of the sample (b). To reduce the influence of material viscoelasticity on the observed behavior of the composite, the tests were performed at a low strain rate of 4×10^{-4} s^{-1}. Upon achieving the critical compression level, the stiffer fibers start developing the buckling shape; the process was captured by two digital cameras (located in front and on the side of the tested samples, as shown in Fig. 1(a)). An example of the single fiber buckling induced configuration obtained from these orthogonal views is shown in Fig. 1(b).

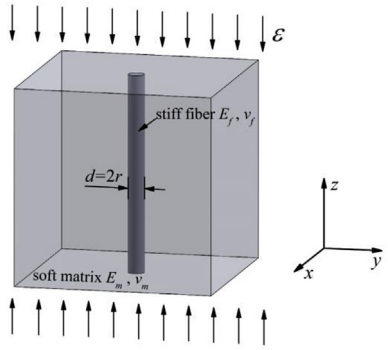

Fig. 2. Sketch of an elastic stiff fiber embedded in a soft matrix subjected to axial compressive load.

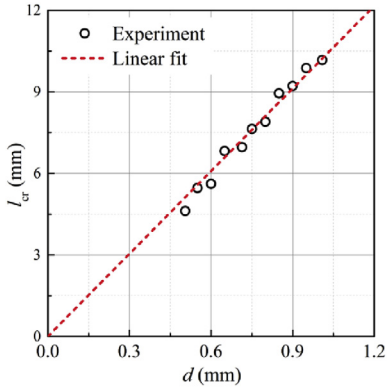

Fig. 4. Dependence of critical wavelength l_{cr} on stiff fiber diameter.

3. Buckling of a single stiff fiber embedded in a soft matrix

We start with the investigation of the buckling of a single stiff fiber embedded in a soft matrix subjected to axial compressive load. The sketch of this system is shown in Fig. 2. E and v refer to the Young's elastic modulus and Poisson's ratio, respectively. Subscripts $(\bullet)_f$ and $(\bullet)_m$ refer to the properties of the stiff fiber and soft matrix, respectively; d refers to the diameter of stiff fiber. Fig. 3 illustrates the development process of instability induced wavy patterns (a) and stress-strain curves (b) for DM fibers with diameters d= 0.50, 0.71, and 1.00 mm. Since the DM fiber buckles almost in the planar configuration, only the view to record the main buckling shape is shown. We observe that the stiff fiber develops wavy patterns, and the critical wavelength and the amplitude of the wavy pattern increase with an increase in stiff fiber diameter (see Fig. 3(a)). Fig. 3(b) shows the corresponding stress–strain curves. Due to the stiff fiber buckling, we observe that the stress–strain curves exhibit softening near to the buckling point. This effect is more significant for the composite with larger stiff fiber diameter (see the dotted black curve in Fig. 3(b)). Similar stress softening phenomenon has been observed in the bulging buckling mode of cylindrical shells under inflation [34,35]. In addition, we note that the composite strength increases with an increase in stiff fiber diameter in pre-buckling and postbuckling regimes.

Next, to clarify the quantitative relation between the critical wavelength and stiff fiber diameter, we plot the critical wavelengths for all tested specimens as a function of stiff fiber diameter in Fig. 4. Interestingly, the critical wavelength has a good linear dependence on the stiff fiber diameter, which will be explained by theoretical analysis in the following discussions.

Here, a theoretical analysis is performed to investigate the buckling mechanisms observed in the experiments. We note that the Winkler foundation model has been frequently utilized to investigate buckling of a single stiff fiber embedded in soft matrix [2,9,10,19]. However, previous works were mostly focused on the systems with high shear modulus contrast (the ratio of stiff fiber to soft matrix shear modulus is larger than 10^5). Here, we study buckling of the 3D printed system with shear modulus contrast of approximately 10^3. We employ the Winkler foundation model, and derive an explicit expression for an accurate approximation for the model, and we further examine the accuracy of model to predict the buckling of single stiff fiber embedded in soft matrix in a wide shear modulus contrast.

Considering the system as a thin and stiff beam supported by a soft matrix, the governing equation for a stiff fiber is given by Ref. [36].

$$E_f I_f \frac{\partial^4 u}{\partial z^4} + E_f S_f \varepsilon \frac{\partial^2 u}{\partial z^2} + Ku = 0 \tag{1}$$

where I_f and S_f are the area moment of inertia and cross-sectional area of the stiff fiber, respectively; ε is the applied axial strain. $u(z) = A\cos(kz)$ is the buckling mode with A and $k = 2\pi/l$ being the amplitude and wavenumber, respectively; l is the wavelength and K is the effective stiffness of soft matrix, which can be expressed as [18].

$$K = \frac{16\pi G_m(1-\nu_m)}{2(3-4\nu_m)K_0(kr) + K_1(kr)kr} \tag{2}$$

where K_0 and K_1 are the modified Bessel functions of the second kind.

Substituting $u(z)$ and Eq. (2) into Eq. (1) yields

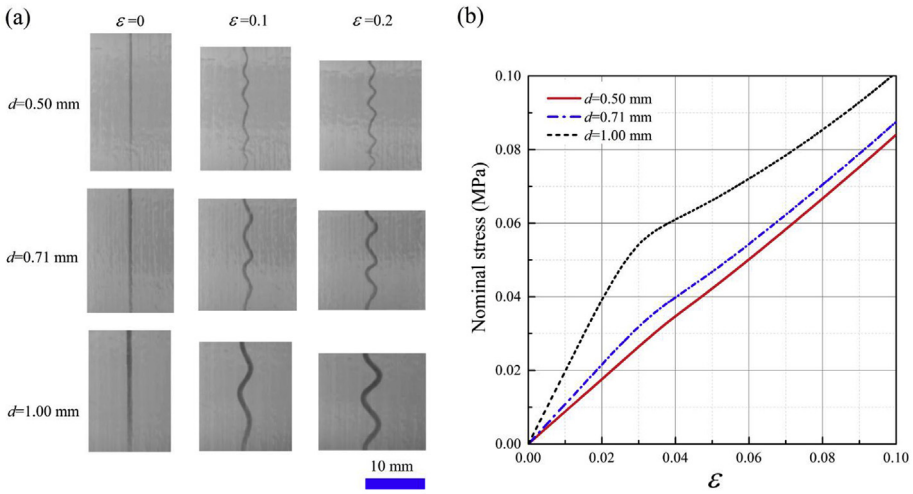

Fig. 3. Development of instability induced wavy patterns (a) and stress-strain curves (b) for a single stiff fiber embedded in a soft matrix.

$$\varepsilon = \frac{(\tilde{k})^2}{4} + \frac{1}{E_f(\tilde{k})^2}\frac{16G_m(1-\nu_m)}{2(3-4\nu_m)K_0(\tilde{k}) + K_1(\tilde{k})\tilde{k}} \tag{3}$$

where $\tilde{k} = kr$ is the normalized wavenumber. The critical strain ε_{cr} corresponding to the onset of buckling can be obtained by minimizing Eq. (3) with respect to $\tilde{k}$; thus, the critical normalized wavenumber $\tilde{k}_{cr}$ depends on the material property of the system only. It also indicates that the critical wavelength has a linear dependence on stiff fiber diameter. This observation agrees well with our experimental results (see Fig. 4).

Assuming the soft matrix to be incompressible ($\nu_m = 0.5$), Eq. (2) can be approximated (see Appendix for details) as

$$K = \frac{4\pi G_m}{-\ln\left(\frac{e^{\gamma-\frac{1}{2}}}{2}\tilde{k}\right)} \tag{4}$$

where $\gamma = 0.577$ is the Euler's constant. We note that the form of Eq. (4) is consistent with the simplified stiffness for incompressible materials obtained by Zhao et al. [10], Brangwynne et al. [2], and Su et al. [19]. However, the coefficient under the logarithm in the denominator is different. We note that the difference is due to the fact that we account for the second term (i.e. $K_1(\tilde{k})\tilde{k}$) in the denominator; this allows us to obtain a more accurate agreement with the exact value of the effective stiffness term for a wider range of shear modulus contrasts. The different approaches for approximation of Eq. (2) are discussed in Appendix.

Then, substitution of Eq. (4) into Eq. (3) yields

$$\varepsilon = \frac{(\tilde{k})^2}{4} + \frac{1}{E_f(\tilde{k})^2}\frac{4G_m}{-\ln\left(\frac{e^{\gamma-\frac{1}{2}}}{2}\tilde{k}\right)} \tag{5}$$

By minimizing Eq. (5) with respect to $\tilde{k}$, the critical wavenumber can be expressed as

$$\tilde{k}_{cr} = \left(\frac{4G_m}{(1+\nu_f)G_f}\right)^{1/4}\left[\frac{1 + 2\ln\left(\frac{e^{\gamma-\frac{1}{2}}}{2}\tilde{k}_{cr}\right)}{-\ln^2\left(\frac{e^{\gamma-\frac{1}{2}}}{2}\tilde{k}_{cr}\right)}\right]^{1/4} \tag{6}$$

since the right-hand side of Eq. (6) changes very slowly with $\tilde{k}_{cr}$, Eq. (6) can be approximated as

$$\log(\tilde{k}_{cr}) = -0.265\log\left(\frac{G_f}{G_m}\right) + 0.265\log\left(\frac{4}{1+\nu_f}\right) \tag{7}$$

Fig. 5 shows the dependence of the normalized critical wavenumber on shear modulus contrast. We observe that the approximate expression given by Eq. (7) agrees well with the numerical solution of Eq. (1) (compare the dashed red line with the continuous black line in Fig. 5), and the theoretical prediction for critical wavenumber shows good accordance with the experimental observations in a wide range of shear modulus contrast. We note that an increase in Poisson's ratio of the stiff fiber material leads to a slight decrease in the normalized critical wavenumber (compare the dashed blue line with the dashed red line in Fig. 5).

In addition, we perform the standard linear buckling analysis through the finite element numerical procedure implemented in COMSOL 5.2a; thus, we obtain numerically the dependence of normalized critical wavenumber on shear modulus contrast.[1] Fig. 5 presents a comparison of the critical wavenumbers obtained by numerical simulations and theoretical analysis (compare the black circular points with black continuous curve), which additionally demonstrates that the obtained Eq. (7) provides an accurate prediction for the critical wavelength of a stiff fiber embedded in a soft matrix within a wide range of shear modulus contrast ($10^2 < G_f/G_m < 10^8$).

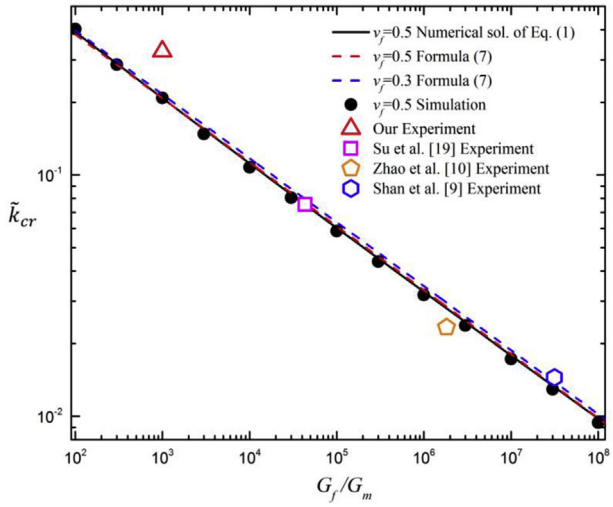

Fig. 5. Normalized critical wavenumber $\tilde{k}_{cr}$ as a function of shear modulus contrast G_f/G_m.

4. Buckling of composites with periodically distributed fibers

Next, we investigate the instability induced pattern formations in composites with fibers periodically distributed in soft matrix. In particular, we study (a) symmetric case of square arrangement of periodically distributed fibers, and (b) case of rectangular arrangements of periodically distributed fibers. We present the experimental results for onset of instabilities in the periodic 3D-printed fiber composites and compare them with the numerical results. In order to numerically identify onset of instabilities and corresponding critical wavelengths, we employ Bloch-Floquet analysis, which is implemented by means of finite element code COMSOL. In the numerical analysis, we consider TP (soft matrix material) and DM (stiff fiber material) as nearly incompressible neo-Hookean materials ($\Lambda/G = 1000$, where Λ is the first Lame constant) with shear modulus contrast $G_f/G_m = 1000$. First, we apply macroscopic deformation by using the periodic displacement boundary conditions imposed on the faces of the unit cell. Once the deformed state is obtained, Bloch-Floquet conditions are imposed on the faces of the unit cell via $\mathbf{u}(\mathbf{X}+\mathbf{R}) = \mathbf{u}(\mathbf{X})e^{-i\mathbf{K}\cdot\mathbf{R}}$, where $\mathbf{X}$ and $\mathbf{u}$ denote the position vector and displacement vector, respectively; $\mathbf{K}$ and $\mathbf{R}$ denote the Bloch wave vector and spatial periodicity in the reference configuration. The corresponding eigenvalue problem with the Bloch-Floquet boundary conditions is solved numerically until a non-trivial zero eigenvalue is detected at a certain deformation level. The corresponding compressive strain and wavenumber are identified as the critical strain ε_{cr} and critical wavenumber k_{cr}, respectively. For more detailed and illustrative description of the numerical instabilities analysis readers are referred to Slesarenko and Rudykh [13]. Note that we distinguish the microscopic and macroscopic (or long wave) instabilities. The microscopic instabilities are associated with onset of instabilities at a finite critical wavelength ($l_{cr} = 2\pi/k_{cr}$, or non-zero critical wavenumber k_{cr}). The macroscopic (or long wave) instabilities are associated with the specific case of $k_{cr}\to 0$, when critical wavelength significantly exceeds the microstructure characteristic size. In this case the onset of macroscopic instabilities can be determined by evaluating the effective tensor of elastic moduli and applying the loss of ellipticity condition [24].

[1] In the numerical model, the soft matrix and stiff fiber are considered as linear elastic material; the geometry of the numerical model is considered as square brick. Considering the computational cost and accuracy, the height of the model is set as $H = 10l_{cr}$ (l_{cr} is estimated by Formula (7)); we note, however, that the choice of the height H in the numerical model may affect the critical wavelength. The side length of the square cross section of the model is set as $W = 150r$ to diminish the effect of the finite size of the sample on critical wavelength.

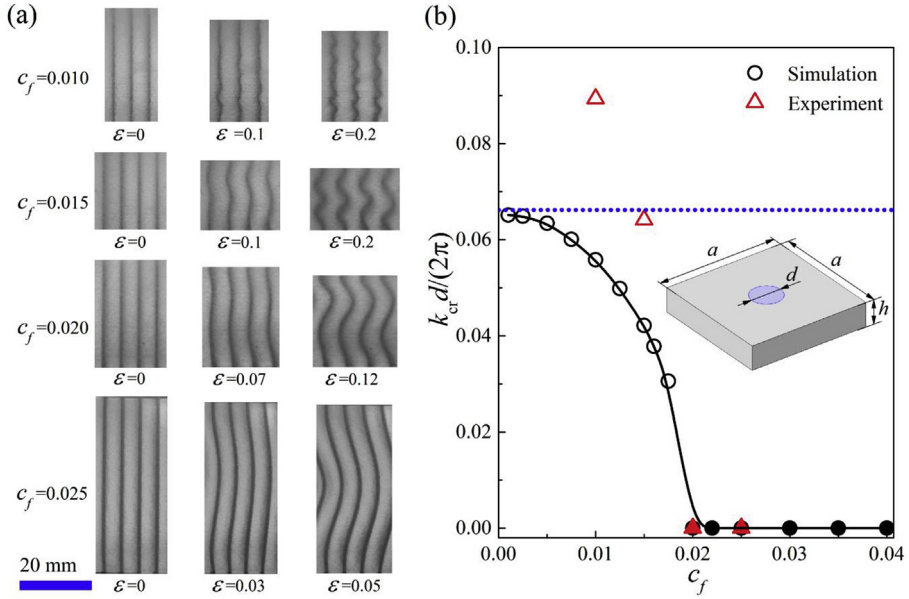

Fig. 6. Development of wavy patterns in fiber composites with square arrangement (a); dependence of critical wavenumber on fiber volume fraction (b). The dotted horizontal line in (b) corresponds to the single fiber analytical result (Eq. (7)).

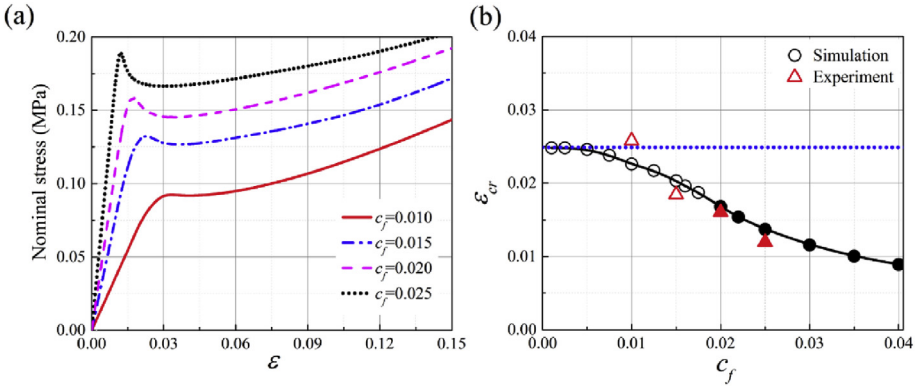

Fig. 7. Experimental stress-strain curves for fiber composites with square arrangement (a), and dependence of the critical strain on fiber volume fraction (b). The dotted horizontal line in (b) corresponds to the single fiber analytical result (Eq. (5)).

4.1. Square arrangement of periodically distributed fibers

Fig. 6 illustrates the development of instability induced wavy patterns (a) and the dependence of critical wavenumber on stiff fiber volume fraction (b) for periodic fiber composite with square arrangement. The representative volume element is shown in the inset of Fig. 6. We observe that the composites with stiff fiber volume fractions $c_f = 0.01$ and 0.015 develop wavy patterns at smaller length scales (typically attributed to microscopic instabilities), while the composite with $c_f = 0.025$ buckles in long wave mode (macroscopic instability). The periodic composite with $c_f = 0.02$ can be arguably assigned to be at the transition zone between the composites that develop microscopic and macroscopic instabilities. Thus, we experimentally observe the transition of the instability induced patterns from small wavelength wavy pattern to long wave mode, as the fiber volume fraction increases. For completeness, we show the dependence of the critical wavenumber on stiff fiber volume fraction obtained through the Bloch-Floquet numerical analysis superimposed on the deformed state in Fig. 6. Here and thereafter, the hollow and solid symbols correspond to the microscopic and macroscopic instabilities, respectively. The circles and triangles denote the numerical and experimental results for periodic fiber composite, respectively; the dashed blue line corresponds to the theoretical result of single fiber composite obtained by Eq. (7). We observe a remarkable agreement of the experimental observations and numerical simulation results. Both experimental observations and numerical simulations show that the critical wavenumber decreases with an increase in stiff fiber volume fraction. When the stiff fiber volume fraction exceeds a certain threshold value ($c_f \approx 0.02$ for $G_f/G_m = 1000$), the fiber composites start developing instabilities in the long wave mode upon achieving the critical level of compressive deformation. The interactions between stiff fibers weaken with a decrease in stiff fiber volume fraction, therefore, we observe that the critical wavenumber of periodic fiber composite in the dilute limit attains the value corresponding to single fiber system (compare the circular points with dashed blue line in Fig. 6(b)).

Fig. 7 shows the experimental stress-strain curves (a), and the dependence of the critical strain (b) for periodic fiber composites with square arrangement. As expected, the stress-strain curves (see Fig. 7 (a)), show that the fiber composites exhibit softening upon achieving the critical strain at which the stiff fibers buckle into wavy patterns. The critical strain is observed to decrease with an increase in stiff fiber volume fraction as shown in Fig. 7 (b). Similar to the observation for critical wavenumber, the critical strain for periodic fiber composites at low stiff fiber volume fraction approaches the critical strain of single fiber system (denoted by the horizontal dotted line in Fig. 7(b)).

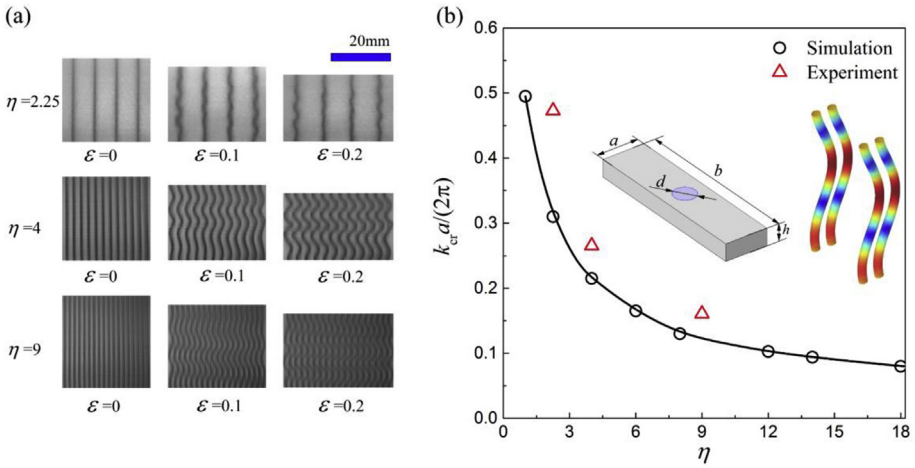

Fig. 8. Development of wavy patterns in fiber composites with rectangle arrangement (a); dependence of critical wavenumber on the periodicity aspect ratio (b).

4.2. Rectangle arrangement of periodically distributed fibers

Next, we investigate the influence of fiber arrangements on the buckling behavior of the periodic fiber composites. In particular, we consider fiber composite with rectangular periodic unit cell. The representative volume element, characterized by aspect ratio $\eta = b/a$, is shown in the inset of Fig. 8. Note that while the aspect ratio is varied, the fiber volume fraction is kept fixed at the value $c_f = 0.01$. In our experiments, the fiber diameter was identical for all composite specimens with different aspect ratios; we also kept fixed the dimensions of the considered specimens and the number of stiff fiber. The development of the wavy pattern in fiber composites with rectangle arrangement is shown in Fig. 8 (a). Similarly to the previously discussed case of periodic square arrangements, the periodic composites with rectangular arrangements of periodic fibers develop wavy patterns, and the amplitude of the wavy pattern significantly increases with an increase in compressive load. However, a change in the periodicity aspect ratio leads to certain cooperative buckling behavior of the fibers such that the wavy patterns develop in the direction, where fibers are close to each other (see the cases for $\eta = 4$, 9 in Fig. 8 (a)). Fig. 8 (b) presents the dependence of critical wavenumbers on aspect ratio. We find that experimental and numerical results show good accordance, especially in the range of high aspect ratio. We also observe that the critical wavenumber decreases with an increase in aspect ratio, and this effect is more significant in the range of small aspect ratio.

Fig. 9 presents the experimental stress-strain curves (a), and the dependence of critical strain (b) for periodic fiber composites with rectangle arrangement. Similar to the observation for fiber composite with square arrangement, we observe that the buckling of the stiff fiber decreases the load capacity of fiber composite (see Fig. 9(a)). In the stable regime, the stiffness of the composites with different periodicity aspect ratios is nearly identical. However, the onset of buckling and the postbuckling behavior changes significantly with a change in the periodicity aspect ratio. Fig. 9 (b) shows the dependence of the critical strain on aspect ratio. We observe that the critical strain decreases with an increase in aspect ratio; thus, the composites with higher aspect ratio require lower levels of compressive deformation to trigger buckling.

5. Conclusion

In this work, we have examined the elastic buckling of single stiff fiber and periodically distributed stiff fiber embedded in a soft matrix subjected to axial compressive loads. First, we experimentally observed the buckling process of a single fiber embedded in soft matrix. We have found that the critical wavelength and the amplitude of the wavy pattern increase with an increase in fiber diameter, and the critical wavelength has a linear dependence on the stiff fiber diameter. Then, based on the Winker foundation model, we derived an explicit expression to predict the buckling wavelength, and further verified the derived expression in a wide range of shear modulus contrast by comparing to experimental data and numerical simulations.

Next, we investigated the elastic buckling of composites with periodically distributed fibers. We experimentally observed the transition of the instability induced patterns from small wavelength wavy pattern to long wave mode, along with the increase of fiber volume fraction. For fiber composites with periodic square arrangement, both experimental and numerical results have showed that the critical wavenumber and critical strain decrease with an increase in fiber volume fraction. For

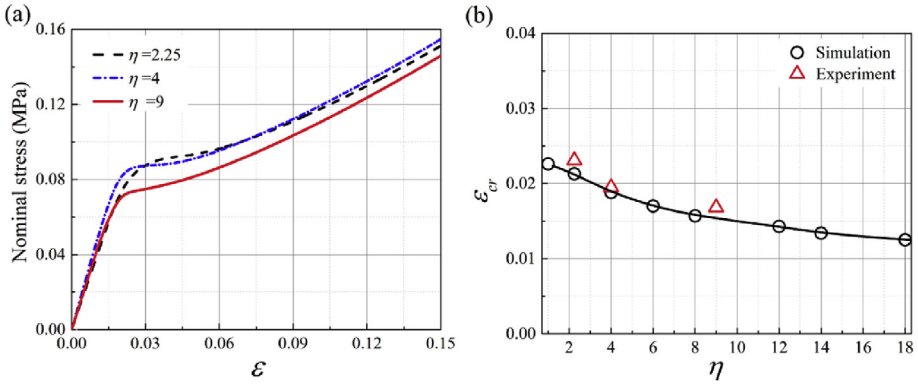

Fig. 9. Experimental stress – strain curves for fiber composites with rectangle arrangement (a), and dependence of the critical strain on the periodicity aspect ratio (b).

fiber composites with rectangular arrangements, we have observed that the stiff fibers develop a cooperative buckle mode in the direction, where the fibers are close to each other; and an increase in aspect ratio leads to a significant decrease in critical wavenumber and critical strain. Thus, various out-of-plane postbuckling wavy patterns can be tailored through design of in-plane fiber arrangements. These findings may be used in design of reconfigurable functional materials, potentially extending the ideas to electro- [37,38] and magnetoactive [39–42] composite materials, tunable acoustic metamaterials [43–45], and other 4D-printed functional materials [46–48].

Acknowledgements

This work was supported by the Israel Science Foundation (grant №1550/15 and 1973/15). JL thanks the support of Lady Davis Fellowship. PG acknowledges the support of the Irwin and Joan Jacobs Fellowship. VS thanks the support of the Technion postdoctoral fellowship.

Appendix. Approximation of the effective stiffness *K* of Winkler foundation model for incompressible material

In this paper, Winkler foundation model is employed to investigate the buckling behavior of a stiff fiber embedded in a soft matrix subjected to a compressive load along the fiber. The matrix is approximated as an array of springs with effective stiffness K acting only in the radial direction. An elastic circular stiff fiber with radius r buckles in the mode of $u(z) = A\cos(kz)$, where A and $k = 2\pi/l$ are the amplitude and wave number, respectively; l is the wavelength. The effective stiffness K can be expressed as [18].

$$K = \frac{16\pi G_m(1-\nu_m)}{2(3-4\nu_m)K_0(\tilde{k}) + K_1(\tilde{k})\tilde{k}} \tag{A1}$$

where $\tilde{k} = kr$, K_0 and K_1 are the modified Bessel functions of the second kind.

We note that for the buckling of an infinite length stiff fiber embedded in a soft matrix, $\tilde{k} \ll 1$, Eq. (A1) can be significantly simplified. At first, $K_0(\tilde{k})$ can be expanded as [49].

$$K_0(\tilde{k}) = -\left\{\ln\left(\frac{\tilde{k}}{2}\right) + \gamma\right\}\left(1 + \frac{\tilde{k}^2}{2^2} + \frac{\tilde{k}^4}{2^2\times 4^2} + \frac{\tilde{k}^6}{2^2\times 4^2\times 6^2} + \cdots\right) + \frac{\tilde{k}^2}{2^2} + \frac{\tilde{k}^4}{2^2\times 4^2}\left(1 + \frac{1}{2}\right) + \frac{\tilde{k}^6}{2^2\times 4^2\times 6^2}\left(1 + \frac{1}{2} + \frac{1}{3}\right) + \cdots \tag{A2}$$

where $\gamma = 0.577$ is the Euler's constant.

Since $\tilde{k} \ll 1$, we neglect the terms of the order higher than 2, then Eq. (A2) is approximated as

$$K_0(\tilde{k}) \approx -\left\{\ln\left(\frac{\tilde{k}}{2}\right) + \gamma\right\} = -\ln\left(\frac{e^{\gamma}}{2}\tilde{k}\right) \tag{A3}$$

Furthermore, $K_1(\tilde{k})\tilde{k}$ has the following approximation [50] when $\tilde{k} \ll 1$,

$$K_1(\tilde{k})\tilde{k} \approx 1 \tag{A4}$$

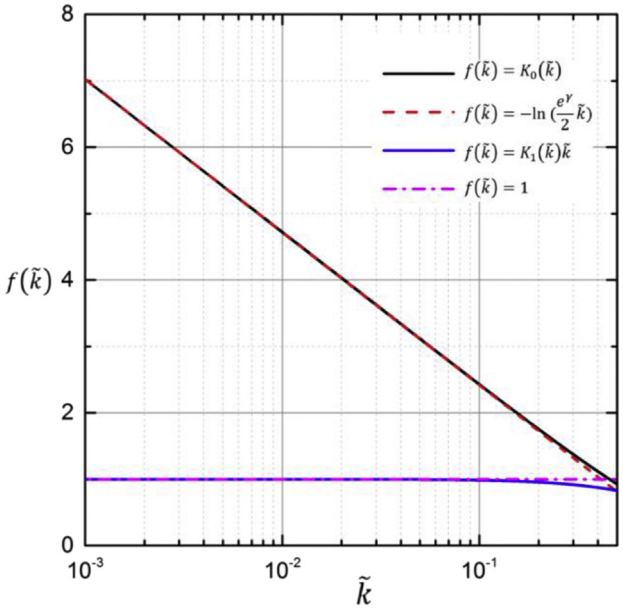

Fig. A1. Comparison of the approximated value with the exact value.

Fig. A1 shows the values of the modified Bessel function of second kind $K_0(\tilde{k})$ and $K_1(\tilde{k})$ and their estimates for the argument $10^{-3} < \tilde{k} < 0.4$. In the considered range, the estimates (A3) and (A4) provide very accurate approximation for the exact values of Bessel functions. For instance, for $\tilde{k} = 0.1$, the estimates (A3) and (A4) produce the values of 2.419 and 1, respectively, while the exact values of $K_0(0.1)$=2.427 and $0.1K_1(0.1)$=0.985. We note that although $K_0(\tilde{k}) \to \infty$ with $\tilde{k} \to 0$, the convergence $K_0(\tilde{k}) \to \infty$ is very slow, for example, $K_0(10^{-10})$= 23.14.

Then, under the soft matrix incompressibility assumption (ν_m = 0.5), substitution of (A3) and (A4) into (A1) yields

$$K \approx \frac{8\pi G_m}{-2\ln\left(\frac{e^{\gamma}}{2}\tilde{k}_{cr}\right)+1} = \frac{4\pi G_m}{-\ln\left(\frac{e^{\gamma-\frac{1}{2}}}{2}\tilde{k}_{cr}\right)} \tag{A5}$$

Different ways to simplify the expression (A1) are reported in the literature (see, for example, Brangwynne et al. [2] and Zhao et al. [10]), where the second term in the denominator is usually neglected. However, according to the results presented in Fig. 5 and Fig. A1, even for relatively high shear modulus contrast, both terms in the denominator of expression (A1) are of the same order, and should not be neglected. For example, for incompressible fiber and soft matrix ($\nu_f = \nu_m = 0.5$), and shear modulus contrast $G_f/G_m = 10^6$, the normalized critical wavenumber $\tilde{k}_{cr}$ is 0.033, and $2K_0(\tilde{k}_{cr}) \approx 7K_1(\tilde{k}_{cr})\tilde{k}_{cr}$. Figure A2 shows a comparison of the exact value of effective stiffness K with estimate (A5) as well as the approximations reported in Refs. [2] and [10] plotted as functions of $\tilde{k}$. We observe that the expression (A5) derived in this work shows an excellent accuracy in approximations of the original expression (A1). Moreover, we note that the inaccuracy of the approximations of the original expression decrease with a decrease in the normalized wavenumber. Since the normalized wavenumber decreases with an increase in shear modulus contrast (see Fig. 5), it means that the approximate expressions ((A5), [2], [10]) provide more accurate results in the range of higher shear modulus contrast.

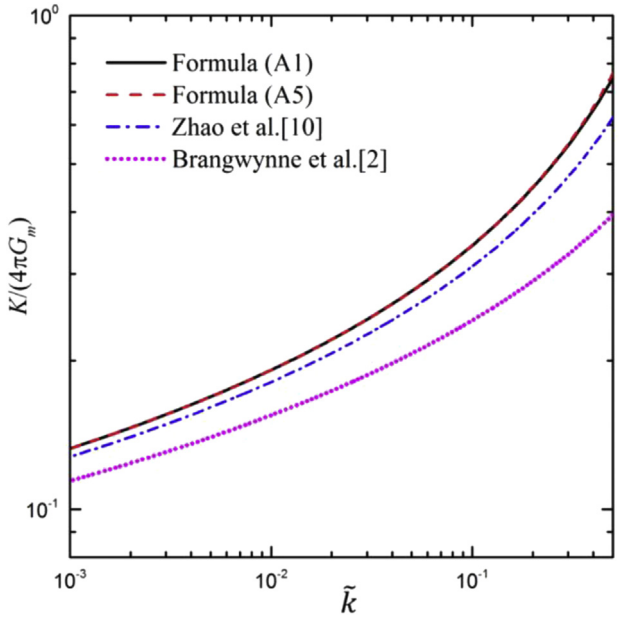

Fig. A2. Comparison of effective stiffness K obtained by the approximate expressions reported in this paper, Brangwynne et al. [2] and Zhao et al. [10] with the original formula (A1).

References

[1] Sammak PJ, Borisy GG. Direct observation of microtubule dynamics in living cells. Nature 1988;332:724–6.
[2] Brangwynne CP, MacKintosh FC, Kumar S, Geisse NA, Talbot J, Mahadevan L, et al. Microtubules can bear enhanced compressive loads in living cells because of lateral reinforcement. J Cell Biol 2006;173:733–41.
[3] Kringelbach ML, Jenkinson N, Owen SLF, Aziz TZ. Translational principles of deep brain stimulation. Nat Rev Neurosci 2007;8:623–35.
[4] L'Heureux N, Pâquet S, Labbé R, Germain L, Auger FA. A completely biological tissue-engineered human blood vessel. Faseb J 1998;12:47–56.
[5] Ku H, Wang H, Pattarachaiyakoop N, Trada M. A review on the tensile properties of natural fiber reinforced polymer composites. Compos B Eng 2011;42:856–73.
[6] Li W, Cai H, Li C, Wang K, Fang L. Micro-mechanics of failure for fatigue strength prediction of bolted joint structures of carbon fiber reinforced polymer composite. Compos Struct 2015;124:345–56.
[7] Spackman CC, Frank CR, Picha KC, Samuel J. 3D printing of fiber-reinforced soft composites: process study and material characterization. J Manuf Process 2016;23:296–305.
[8] Beloshenko V, Voznyak Y, Voznyak A, Savchenko B. New approach to production of fiber reinforced polymer hybrid composites. Compos B Eng 2017;112:22–30.
[9] Shan WL, Chen Z, Broedersz CP, Gumaste AA, Soboyejo WO, Brangwynne CP. Attenuated short wavelength buckling and force propagation in a biopolymer-reinforced rod. Soft Matter 2013;9:194–9.
[10] Zhao Y, Li J, Cao YP, Feng X-Q. Buckling of an elastic fiber with finite length in a soft matrix. Soft Matter 2016;12:2086–94.
[11] Andrianov IV, Kalamkarov AL, Weichert D. Buckling of fibers in fiber-reinforced composites. Compos B Eng 2012;43:2058–62.
[12] Lu H, Li J, Nie C, Duan B, Yin W, Yao Y, et al. Study on buckling response in electrospun fiber with periodic structure. Compos B Eng 2017;113:270–7.
[13] Slesarenko V, Rudykh S. Microscopic and macroscopic instabilities in hyperelastic fiber composites. J Mech Phys Solid 2017;99:471–82.
[14] Greco F, Lonetti P, Luciano R, Nevone Blasi P, Pranno A. Nonlinear effects in fracture induced failure of compressively loaded fiber reinforced composites. Compos Struct 2018;189:688–99.
[15] Kong XY, Wang ZL. Spontaneous polarization-induced nanohelixes, nanosprings, and nanorings of piezoelectric nanobelts. Nano Lett 2003;3:1625–31.
[16] Gao C, Li Y. Tuning the wrinkling patterns of an interfacial/coating layer via a regulation interphase. Int J Solid Struct 2017;104–105:92–102.
[17] Silverberg JL, Noar RD, Packer MS, Harrison MJ, Henley CL, Cohen I, et al. 3D imaging and mechanical modeling of helical buckling in Medicago truncatula plant roots. Proc Natl Acad Sci Unit States Am 2012;109:16794–9.
[18] Herrmann LR, Mason WE, Chan STK. Response of reinforcing wires to compressive states of stress. J Compos Mater 1967;1:212–26.
[19] Su T, Liu J, Terwagne D, Reis PM, Bertoldi K. Buckling of an elastic rod embedded on an elastomeric matrix: planar vs. non-planar configurations. Soft Matter 2014;10:6294–302.
[20] Chen Y, Liao X, Liu Y, Chen X. Helical buckling of wires embedded in a soft matrix under axial compression. Extrem Mech Lett 2017;17:71–6.
[21] Winkler E. Die Lehre von der Elastizität und Festigkeit. Verlag; 1867. H. Dominikus, Prag.
[22] Rosen BW. Mechanics of composite strengthening. Fibre Composite Materials. Am. Soc. Met., Ohio. 1965. p. 37–75.
[23] Triantafyllidis N, Maker BN. On the comparison between microscopic and macroscopic instability mechanisms in a class of fiber-reinforced composites. J Appl Mech 1985;52:794.
[24] Geymonat G, Muller S, Triantafyllidis N. Homogenization of nonlinearly elastic materials, microscopic bifurcation and macroscopic loss of rank-one convexity. Arch Ration Mech Anal 1993;122:231–90.
[25] Merodio J, Ogden RW. Mechanical response of fiber-reinforced incompressible non-linearly elastic solids. Int J Non Lin Mech 2005;40:213–27.
[26] Merodio J, Ogden RW. Material instabilities in fiber-reinforced nonlinearly elastic solids under plane deformation. Arch Mech 2002;54:525–52.
[27] Merodio J, Ogden RW. Instabilities and loss of ellipticity in fiber-reinforced compressible non-linearly elastic solids under plane deformation. Int J Solid Struct 2003;40:4707–27.
[28] Merodio J, Ogden RW. Remarks on instabilities and ellipticity for a fiber-reinforced

compressible nonlinearly elastic solid under plane deformation. Q Appl Math 2005;63:325–33.
[29] Agoras M, Lopez-Pamies O, Ponte Castañeda P. Onset of macroscopic instabilities in fiber-reinforced elastomers at finite strain. J Mech Phys Solid 2009;57:1828–50.
[30] Rudykh S, Debotton G. Instabilities of hyperelastic fiber composites: micromechanical versus numerical analyses. J Elasticity 2012;106:123–47.
[31] Greco F, Leonetti L, Medaglia CM, Penna R, Pranno A. Nonlinear compressive failure analysis of biaxially loaded fiber reinforced materials. Compos B Eng 2018 https://doi.org/10.1016/j.compositesb.2018.04.006.
[32] Li Y, Kaynia N, Rudykh S, Boyce MC. Wrinkling of interfacial layers in stratified composites. Adv Eng Mater 2013;15:921–6.
[33] Slesarenko V, Rudykh S. Harnessing viscoelasticity and instabilities for tuning wavy patterns in soft layered composites. Soft Matter 2016;12:3677–82.
[34] Merodio J, Haughton DM. Bifurcation of thick-walled cylindrical shells and the mechanical response of arterial tissue affected by Marfan's syndrome. Mech Res Commun 2010;37:1–6.
[35] Haughton DM, Merodio J. The elasticity of arterial tissue affected by Marfan's syndrome. Mech Res Commun 2009;36:659–68.
[36] Timoshenko SP, Gere JM. Theory of elastic stability. second ed. New York: McGraw-Hill; 1961.
[37] Goshkoderia A, Rudykh S. Electromechanical macroscopic instabilities in soft dielectric elastomer composites with periodic microstructures. Eur J Mech Solid 2017;65:243–56.
[38] Balakrisnan B, Nacev A, Smela E. Design of bending multi-layer electroactive polymer actuators. Smart Mater Struct 2015;24:045032.
[39] Ciambella J, Stanier DC, Rahatekar SS. Magnetic alignment of short carbon fibres in curing composites. Compos B Eng 2017;109:129–37.
[40] Psarra E, Bodelot L, Danas K. Two-field surface pattern control via marginally stable magnetorheological elastomers. Soft Matter 2017;13:6576–84.
[41] Ciambella J, Favata A, Tomassetti G. A nonlinear theory for fibre-reinforced magneto-elastic rods. Proc R Soc A Math Phys Eng Sci 2018;474:20170703.
[42] Goshkoderia A, Rudykh S. Stability of magnetoactive composites with periodic microstructures undergoing finite strains in the presence of a magnetic field. Compos B Eng 2017;128:19–29.
[43] Bertoldi K, Boyce MC. Wave propagation and instabilities in monolithic and periodically structured elastomeric materials undergoing large deformations. Phys Rev B 2008;78:184107.
[44] Galich PI, Fang NX, Boyce MC, Rudykh S. Elastic wave propagation in finitely deformed layered materials. J Mech Phys Solid 2017;98:390–410.
[45] Galich PI, Rudykh S. Shear wave propagation and band gaps in finitely deformed dielectric elastomer laminates: long wave estimates and exact solution. J Appl Mech 2017;84:091002.
[46] Che K, Yuan C, Wu J, Jerry Qi H, Meaud J. Three-dimensional-printed multistable mechanical metamaterials with a deterministic deformation sequence. J Appl Mech 2016;84:011004.
[47] Ding Z, Weeger O, Qi HJ, Dunn ML. 4D rods: 3D structures via programmable 1D composite rods. Mater Des 2018;137:256–65.
[48] Yuan C, Roach DJ, Dunn CK, Mu Q, Kuang X, Yakacki CM, et al. 3D printed reversible shape changing soft actuators assisted by liquid crystal elastomers. Soft Matter 2017;13:5558–68.
[49] Spiegel MR, Lipschutz S, Liu J. Mathematical handbook of formulas and tables. second ed. McGraw-Hill; 1998. p. 137–9.
[50] Abramowitz M, Stegun I. Handbook of mathematical functions with formulas, graphs, and mathematical tables. National Institute of Standards and Technology; 1964. p. 375.